Eden, DJ, Moore, TJT, Morgan, LK, Thompson, MA and Urquhart, JS

 Star formation in Galactic spiral arms and the interarm regions

http://researchonline.ljmu.ac.uk/id/eprint/8230/

Article

For more information please contact researchonline@ljmu.ac.uk

Star formation in Galactic spiral arms and the interarm regions

D. J. Eden,[1]⋆ T. J. T. Moore,[1] L. K. Morgan,[1] M. A. Thompson[2] and J. S. Urquhart[3]

[1]*Astrophysics Research Institute, Liverpool John Moores University, Twelve Quays House, Egerton Wharf, Birkenhead CH41 1LD, UK*
[2]*Centre for Astrophysics Research, Science & Technology Research Institute, University of Hertfordshire, College Lane, Hatfield, Herts AL10 9AB, UK*
[3]*Max-Planck-Institut für Radioastronomie, Auf dem Hügel 69, D-53121 Bonn, Germany*

ABSTRACT

The line of sight through the Galactic plane between longitudes $l = 37°83$ and $42°50$ allows for the separation of Galactic Ring Survey molecular clouds into those that fall within the spiral arms and those located in the interarm regions. By matching these clouds in both position and velocity with dense clumps detected in the mm continuum by the Bolocam Galactic Plane Survey, we are able to look for changes in the clump formation efficiency (CFE), the ratio of clump to cloud mass, with Galactic environment. We find no evidence of any difference in the CFE between the interarm and spiral-arm regions along this line of sight. This is further evidence that, outside the Galactic Centre region, the large-scale structures of the Galaxy play little part in changing the dense, potentially star-forming structures within molecular clouds.

Key words: stars: formation – ISM: clouds – Galaxy: kinematics and dynamics.

1 INTRODUCTION

The role played by spiral arms in triggering or regulating star formation is ambiguous. Significant increases in the efficiency of molecular cloud formation from the neutral interstellar medium (ISM) in the spiral-arm entry shock have been observed (Heyer & Terebey 1998) and explained theoretically (Dobbs, Bonnell & Pringle 2006). Since such shocks will be stronger at Galactocentric radii inside the corotation radius (which for the Milky Way is thought to be at around 8 kpc; Lépine et al. 2011), it has been suggested that supernovae, rather than spiral structure, may be the dominant mechanism in regulating the state of the ISM and, hence, the mode, rate and efficiency of star formation in the outer Galaxy (Dib et al. 2009).

Other theoretical predictions suggest that spiral arms may be largely organizing features which mainly slows down the ISM gas in its orbit, but that this may allow larger giant molecular clouds (GMCs) to form (Dobbs, Burkert & Pringle 2011). A study by Roman-Duval et al. (2010) found similar results using data from the Galactic Ring Survey (GRS), implying that clouds in interarm regions dissipate more quickly. If true, this may affect the mass function of stellar clusters that form, since radiative heating should suppress fragmentation in higher column density clouds without significantly affecting the overall star formation rate (SFR) or efficiency (Krumholz et al. 2010). Moore et al. (2012) found that around 70 per cent of the increase in SFR density in spiral arms in the Galaxy is due to simple crowding. The remainder can either be due to rises in star formation efficiency (SFE) or increases in the mean luminosity of massive young stellar objects.

These models and results are apparently contradicted, however, by other evidence showing that spiral arms have little effect. For instance, Foyle et al. (2010) found little difference in either the ratio of molecular gas to H I or the SFE in and out of the arms of two external spiral galaxies. Eden et al. (2012), examining the fraction of molecular gas in dense clumps within clouds, found no difference between clouds in the Scutum-arm tangent and those in the foreground and background structures on the same line of sight. This implies a constant conversion of molecular gas into dense, star-forming structures regardless of environment.

To determine the effect of Galactic spiral arms on star formation, we need a model of the Galactic structure. The consensus, from the mapping of distances to observed H II regions, is that the spiral structure of the Galaxy can be represented by a four-arm model (e.g. Russeil 2003; Paladini, Davies & De Zotti 2004) but the geometry of these arms is not agreed upon. The four main arms – Norma, Sagittarius, Perseus and Scutum–Centaurus – are added to by the near and far 3 kpc arms. The Milky Way also has a central bar which can be split into a 3.1–3.5 kpc Galactic bar at an angle of 20° with respect to the Galactic Centre–Sun axis (Binney et al. 1991; Blitz & Spergel 1991; Dwek et al. 1995) and a non-symmetric structure, the long bar (Hammersley et al. 2000), at an angle of 44° ± 10° with a Galactic radius of 4.4 ± 0.5 kpc, as revealed by star counts from the *Spitzer* GLIMPSE survey (Benjamin et al. 2005).

In this paper, we compare the fraction of molecular gas mass in dense, potentially star-forming clumps in Galactic spiral arms to that of clouds in the interarm zones. This is the clump formation efficiency (CFE), which is the dense-clump analogue (or precursor) of the SFE. The region covered by this study is the slice of the Galactic plane $l = (37°83–42°50)$, $|b| ≤ 0°5$, which will hereafter be referred to as the $l = 40°$ region. This line of sight is located between the Scutum–Centaurus tangent (at $l ≈ 30°$) and the

⋆ E-mail: dje@astro.livjm.ac.uk

Sagittarius tangent ($l \approx 50°$), and intersects the Sagittarius arm twice. The $l = 40°$ region is suitable for comparisons between spiral-arm and interarm star formation, as multiple zones of each type are observed along the line of sight but there is no arm tangent, meaning that the arms are well separated. Populations of molecular clouds can be attributed to two intersections of the Sagittarius arm, the edge of the Scutum–Centaurus tangent and the Perseus arm, with corresponding interarm regions in between. The interarm region between the Scutum–Centaurus and Sagittarius arms falls at the tangent point in this line of sight, so it is not subject to distance ambiguities which can affect the results. This line of sight is also a molecular-rich interarm region (Sawada et al. 2012). In the next section (Section 2), we give a brief overview of the data sets used. Methods for assigning distance to Bolocam Galactic Plane Survey (BGPS) sources which cannot be associated with GRS clouds are described in Section 3. Section 4 contains the results and analysis and Section 5 is the discussion of the results. Section 6 is a summary of the conclusions.

2 DATA SETS AND OBSERVATIONS

2.1 Galactic Ring Survey

The GRS (Jackson et al. 2006) mapped ^{13}CO $J = 1 \rightarrow 0$ emission in Galactic longitude from $l = 18°$ to $55°.7$ and $|b| \leq 1°$, covering a total area of 75.4 deg^2, with a velocity range of -5 to 135 km s^{-1} for $l \leq 40°$ and -5 to 85 km s^{-1} for $l > 40°$ at an rms sensitivity of ~ 0.13 K. The GRS is fully sampled with a 46 arcsec angular resolution on a 22 arcsec grid and has a spectral resolution of 0.21 km s^{-1}. The velocity range limits detections to within the solar circle.

A catalogue of 829 molecular clouds within the GRS region, identified using the CLUMPFIND algorithm (Williams, de Geus & Blitz 1994) was published by Rathborne et al. (2009). Roman-Duval et al. (2009) determined distances to 750 of these clouds using H ɪ self-absorption (HISA) to resolve the kinematic distance ambiguities. This cloud distance catalogue was complemented by the work of Roman-Duval et al. (2010), who made use of ^{12}CO $J = 1 \rightarrow 0$ emission from the University of Massachusetts–Stony Brook survey (Clemens et al. 1986; Sanders et al. 1986) to derive the masses, as well as other physical properties, of 580 molecular clouds. A power-law relation between their radii and masses was produced to allow the masses for a further 170 molecular clouds to be estimated. The associated cloud mass uncertainties are also catalogued. The clouds catalogued are those made up of the lower density, more diffuse molecular material within the ISM.

The molecular cloud mass completeness limit of the GRS as a function of distance is $M_{min} = 50d^2$ M$_\odot$, where d is the distance in kpc. Therefore, the survey is complete above a mass of 4×10^4 M$_\odot$ out distances of 15 kpc (Roman-Duval et al. 2010), so it is believed to be complete for the distances probed by this study.

2.2 The Bolocam Galactic Plane Survey

The Bolocam Galactic Plane Survey (BGPS; Aguirre et al. 2011) mapped 133 deg^2 of the north Galactic plane in the continuum at 271.1 GHz ($\lambda = 1.1$ mm) with a bandwidth of 46 GHz, an rms noise level of 11–53 mJy beam^{-1} and an effective angular resolution of 33 arcsec. The survey was continuous from $l = -10°.5$ to $90°.5$, $|b| \leq 0°.5$ with cross-cuts which flare out to $|b| \leq 1°.5$ at $l = 3°$, $15°$, $30°$ and $31°$ and towards the Cygnus X massive star-forming region at $l = 75°.5$–$87°.5$. A further 37 deg^2 was observed towards

targeted regions in the outer Galaxy, bringing the total survey area to 170 deg^2.

A custom source extraction algorithm, Bolocat, was designed and utilized to extract 8358 sources, with a catalogue 98 per cent complete from 0.4 to 60 Jy over all sources with object size ≤ 3.5 arcmin. The completeness limit of the survey varies as a function of longitude, with the flux density completeness limit taken as five times the median rms noise level in $1°$ bins (Rosolowsky et al. 2010). They concluded that the extracted sources were best described as molecular clumps – large, dense, bound regions within which stellar clusters and large systems form.

The flux densities for each source also require a multiplication by a factor of 1.5 to provide consistency with other data sets from MAMBO and SIMBA surveys (Aguirre et al. 2011).

2.3 ^{13}CO $J = 3 \rightarrow 2$ data

The higher energy transition of $J = 3 \rightarrow 2$ traces higher density gas than the $J = 1 \rightarrow 0$ transition. It has a critical density of $\gtrsim 10^4$ cm^{-3}, compared to 10^2–10^3 cm^{-3} for $J = 1 \rightarrow 0$, and $E(J = 3)/k = 32.8$ K so is also biased towards warmer gas. $J = 3 \rightarrow 2$ is therefore less ambiguous than $J = 1 \rightarrow 0$ in identifying the emission from dense, star-forming clumps, and is useful in separating multiple emission components within a spectrum along a particular line of sight.

The $l = 40°$ region was mapped in ^{13}CO $J = 3 \rightarrow 2$ (330.450 GHz) with the Heterodyne Array Receiver Programme (HARP) detector at the James Clerk Maxwell Telescope on Mauna Kea, Hawaii. HARP has 16 receptors, each with a beam size of ~ 14 arcsec, separated by 30 arcsec and operates in the 325–375 GHz band (Buckle et al. 2009). Observations were made in two parts, $l = 37°.83$–$40°.5$ in 2010 and $l = 40°.5$–$42°.5$ in 2011. The Galactic latitude range of these observations is $|b| \leq 0°.5$, with a velocity range of -50 to 150 km s^{-1}. The increased velocity range allows for sources outside of the solar circle to be identified. The data were used only to provide the velocity of the peaks in the spectra extracted. The observations and reduction procedure will be discussed in more detail in a later paper.

2.4 The Very Large Array Galactic Plane Survey

The Very Large Array Galactic Plane Survey (VGPS; Stil et al. 2006) mapped H ɪ and 21 cm continuum emission in Galactic longitude from $l = 18°$ to $67°$ and in Galactic latitude from $|b| \leq 1°.3$ to $|b| \leq 2°.3$. The survey has an angular resolution of 1 arcmin, with a spectral resolution of 1.56 km s^{-1} and an rms sensitivity of 2 K. These data will be used for distance determinations, as described in Section 3.

3 BGPS SOURCE DISTANCE DETERMINATION

The $l = 40°$ region contains 67 GRS catalogue clouds (Rathborne et al. 2009) in the longitude range $l = 37°.83$–$42°.50$ and latitudes $|b| \leq 0°.5$ (59 with distances; Roman-Duval et al. 2009). The upper longitude limit is set by the current extent of the HARP survey data, while the latitude range approximately corresponds to the BGPS at these longitudes. 229 BGPS sources were identified within the target area. We assigned velocities to these by extracting spectra from the HARP data cubes at the BGPS catalogue position. For sources whose spectra displayed more than one significant emission peak, the strongest emission feature was chosen (Urquhart et al. 2007), which was the case for less than 5 per cent of sources. The BGPS actually detected sources outside the nominal latitude range, to

approximately $|b| \leq 0°.55$. Five of these are included in this study. The GRS data were used as the primary indicator for those sources which fell outside of the HARP latitude range.

The positions and assigned velocities of the BGPS sources were matched to those derived for the clouds in the Rathborne et al. (2009) catalogue, with positional tolerances of 5×5 resolution elements in the $l \times b$ directions, which corresponds to 110 arcsec in each direction in the GRS data on which the Rathborne et al. (2009) catalogue is based. The velocity tolerance was taken to be the full width at half-maximum of the ^{13}CO $J = 1 \rightarrow 0$ emission line from the aforementioned catalogue. This resulted in cloud associations for 186 BGPS sources. 23 of these were associated with distance-less clouds, the remaining 163 BGPS sources were assigned the catalogued distances (Roman-Duval et al. 2009) of the associated GRS clouds.

This left $229 - 186 = 43$ BGPS detections unassociated with GRS clouds, since no matching clouds were found in the catalogue. Nine of these sources were found to have velocities outside of the range of the GRS, by using the extended velocity range of the HARP data. These sources were assumed to lie in clouds outside the solar circle, probably in the Norma–Outer Arm and as such they are not catalogued by Rathborne et al. (2009). Hence, no mass and no CFE is calculated for these BGPS sources. The remaining 34 sources without associated clouds but within the solar circle had two possible reasons for their lack of assignment: incorrect kinematic velocities or because the host clouds were not identified by the GRS survey. Velocity assignments made initially using the $J = 3 \rightarrow 2$ data were checked against the $J = 1 \rightarrow 0$ data and found to be consistent in all cases. However, where cloud associations had not been found, we checked the velocities of any secondary (i.e. fainter) emission features in the $J = 1 \rightarrow 0$ spectra that were not present in the $J = 3 \rightarrow 2$ data and found a further 10 associations, with 1 of these in a distance-less cloud.

In order to look for velocity information for the remaining 24 unassociated sources, we produced velocity-integrated maps of the ^{13}CO $J = 1 \rightarrow 0$ emission from the public GRS data. Emission was found for all 24 sources, arising in either relatively bright, compact regions, some with very small velocity ranges or from filamentary-type clouds. These likely fell below the detection criteria used by Rathborne et al. (2009) of Δl or $\Delta b \geq 6$ arcmin or $\Delta V \geq 0.6$ km s^{-1}. We found that 10 BGPS sources are coincident with 10 small, low-velocity-dispersion clouds, with 14 BGPS sources falling in 11 filamentary-type clouds.

Table 1 displays a summary of the GRS cloud–BGPS associations, displaying the associations for individual clouds (only a small portion of the data is provided here, with the full list of 196 BGPS sources available as Supporting Information to the online paper).

There are associated errors with these distance determinations. A full discussion of the distance determinations involved with the GRS clouds and velocity assignments can be found in Roman-Duval et al. (2009), but for clouds at a distance further than 3 kpc, the error on the kinematic distances is at most 30 per cent for the near distance and less than 20 per cent at the far distance. These uncertainties assume that the distance ambiguity has been correctly resolved.

The method used to assign kinematic distances to BGPS sources not associated with GRS catalogued clouds is as outlined in Eden et al. (2012). The rotation curve of Brand & Blitz (1993) is used to assign two kinematic distances to each BGPS source. A single kinematic distance is then decided upon via the HISA method (e.g. Anderson & Bania 2009; Roman-Duval et al. 2009) using H I spectra from the VGPS.

Table 1. Summary of GRS cloud parameters and BGPS source associations. Only a small portion of the data is provided here. The full list of 196 BGPS sources is available as Supporting Information to the online paper.

GRS cloud name	GRS V_{LSR} (km s^{-1})	GRS D (kpc)	BGPS source ID	BGPS l (°)	BGPS b (°)
G039.29−00.61	64.55	4.43	5973	39.27	−0.59
G039.29−00.61	64.55	4.43	5989	39.54	−0.37
G039.34−00.26	69.65	4.93	5968	39.16	−0.17
G039.34−00.26	69.65	4.93	5976	39.29	−0.20
G039.34−00.26	69.65	4.93	5980	39.39	−0.14
G039.34−00.26	69.65	4.93	5982	39.48	−0.29
G039.34−00.31	65.82	4.55	5978	39.33	−0.32
G039.34−00.31	65.82	4.55	5981	39.44	−0.19
G039.34−00.31	65.82	4.55	5993	39.59	−0.21
G039.49−00.21	17.40	–	5979	39.37	−0.18
G039.49−00.21	17.40	–	5984	39.49	−0.18
G039.49−00.21	17.40	–	5986	39.50	−0.20
G039.49−00.21	17.40	–	5997	39.67	−0.16
G039.59−00.01	43.29	2.85	5990	39.56	−0.03
G039.59−00.01	43.29	2.85	5991	39.57	−0.04
G039.59−00.01	43.29	2.85	5992	39.57	0.01

Table 2. The unassociated BGPS sources and their derived kinematic distances.

BGPS source ID	l (°)	b (°)	V_{LSR} (km s^{-1})	D (kpc)
5916	38.47	−0.07	24.80	11.62
5927	38.67	0.23	29.22	11.29
5955	38.91	−0.15	58.36	3.92
5963	38.98	−0.08	16.89	1.13
5966	39.05	0.22	7.11	12.80
5969	39.18	−0.24	58.76	9.22
5988	39.53	−0.20	51.53	3.47
6000	39.69	−0.16	51.32	3.46
6007	39.90	−0.08	73.43	7.71
6010	39.92	−0.37	59.40	8.99
6013	39.96	−0.15	57.49	9.12
6015	40.07	0.18	9.29	12.45
6020	40.22	−0.03	9.81	12.38
6028	40.60	−0.10	65.11	4.58
6031	40.74	0.16	16.29	1.08
6033	40.81	−0.42	79.05	6.43
6048	41.15	−0.08	49.03	3.35
6071	41.51	−0.11	63.48	4.53
6080	41.73	−0.25	70.28	5.38
6081	41.73	−0.24	70.59	5.44
6083	41.76	−0.06	26.50	1.80
6086	41.88	0.47	20.55	11.28
6087	41.88	0.49	21.19	11.23
6096	42.10	0.35	20.76	1.39

Of the 24 BGPS sources not associated with GRS catalogued clouds but found to be coincident with small clouds or filaments in the GRS data, 13 were assigned the near kinematic distance, with 11 found to be at the far kinematic distance. Table 2 displays the unassociated sources and their derived kinematic distances. The clouds with which these sources are associated have no calculated CFE, since there is no CO-derived cloud mass. The CO detections of these sources have only been used to obtain local standard of rest (LSR) velocities. The current calculations of CFE contain all the

GRS catalogued clouds, even those without any associated BGPS sources. Calculating a CFE that includes the small or filamentary clouds would involve producing a full catalogue of them, as well as a solid definition of what constitutes a small cloud as opposed to just an overdensity within the wispy CO background material.

The molecular clouds associated with 196 BGPS sources have been identified. In Table 3, we present the GRS clouds with the number of associated BGPS sources. There are 67 molecular clouds from the Rathborne et al. (2009) catalogue in the $l = 40°$ region. We have associated 47 of these clouds with 196 BGPS sources, with only 9 having just a single associated BGPS source.

In Fig. 1, we present a histogram of the number of BGPS sources found in each GRS molecular cloud. All but 4 of these clouds are

Table 3. Summary of GRS cloud parameters, number of BGPS source associations and the associated BGPS source masses.

GRS cloud name	l (°)	b (°)	V_{LSR} (km s^{-1})	M_{cloud} (M$_\odot$)	D (kpc)	No. BGPS sources	M_{clumps} (M$_\odot$)	CFE (per cent)	ΔCFE (per cent)	Arm/ interarm
G037.59−00.66	37.59	−0.66	20.76	2150	1.45	0	0	0.0	0.0	a
G037.69+00.09	37.69	0.09	84.10	297 000	6.70	5	5830	2.0	1.0	i
G037.74−00.06	37.74	−0.06	86.65	290 000	6.70	11	7288	2.5	0.4	i
G037.74−00.46	37.74	−0.46	74.75	17 800	5.25	0	0	0.0	0.0	a
G037.74+00.19	37.74	0.19	45.40	–	–	0	–	–	–	–
G037.79+00.24	37.79	0.24	47.54	9160	10.32	0	0	0.0	0.0	i
G037.84−00.41	37.84	−0.41	64.97	106 000	9.05	1	554	0.5	0.3	a
G037.89−00.21	37.89	−0.21	13.54	1400	1.05	0	0	0.0	0.0	a
G037.89−00.41	37.89	−0.41	61.15	134 000	9.32	2	15 000	11.2	4.6	a
G038.04−00.26	38.04	−0.26	13.11	145	1.02	0	0	0.0	0.0	a
G038.04+00.19	38.04	0.19	42.87	382	2.80	1	371	97.1	52.6	i
G038.19−00.16	38.19	−0.16	62.85	34 900	4.22	3	876	2.5	1.2	a
G038.24−00.16	38.24	−0.16	65.40	125 000	8.93	5	4920	3.9	1.6	a
G038.49+00.14	38.49	0.14	17.36	1380	1.27	8	133	9.6	4.5	a
G038.54−00.06	38.54	−0.06	16.94	1370	1.25	7	87	6.4	2.9	a
G038.59−00.41	38.59	−0.41	19.06	1210	1.35	3	67.5	5.6	2.7	a
G038.69−00.06	38.69	−0.06	36.07	1700	2.38	2	49.6	2.9	1.6	i
G038.69−00.11	38.69	−0.11	42.02	619	2.75	0	0	0.0	0.0	i
G038.69+00.44	38.69	0.44	16.94	215	1.25	0	0	0.0	0.0	a
G038.74−00.46	38.74	−0.46	50.52	20 800	9.93	5	9220	44.3	17.6	i
G038.79−00.51	38.79	−0.51	66.25	128 000	8.70	7	6310	4.9	2.0	a
G038.89−00.26	38.89	−0.26	44.14	1850	2.90	3	374	20.2	7.2	i
G038.94−00.46	38.94	−0.46	41.59	488 000	10.50	15	53 000	10.9	2.7	i
G038.99−00.41	38.99	−0.41	60.72	297 000	9.12	3	2290	0.8	0.3	a
G039.09+00.49	39.09	0.49	22.89	32 000	11.60	2	3750	11.7	5.7	a
G039.19+00.49	39.19	0.49	28.80	–	–	0	–	–	–	–
G039.24−00.61	39.24	−0.61	16.50	–	–	3	–	–	–	–
G039.24−00.06	39.24	−0.06	22.46	22 000	11.60	2	28 310	128.7	55.0	a
G039.29−00.61	39.29	−0.61	64.55	16 100	4.43	2	664	4.1	2.1	a
G039.34−00.26	39.34	−0.26	69.65	34 300	4.93	4	1770	5.2	2.0	a
G039.34−00.31	39.34	−0.31	65.82	25 400	4.55	3	1290	5.1	2.2	a
G039.49+00.29	39.49	0.29	42.44	301	2.80	0	0	0.0	0.0	i
G039.49−00.21	39.49	−0.21	17.40	–	–	4	–	–	–	–
G039.54+00.29	39.54	0.29	15.20	–	–	0	–	–	–	–
G039.59−00.01	39.59	−0.01	43.29	778	2.85	3	117	15.0	8.7	i
G039.69−00.56	39.69	−0.56	83.25	49 500	6.55	2	1010	2.0	1.0	i
G039.89−00.21	39.89	−0.21	57.80	–	–	14	–	–	–	–
G040.09−00.51	40.09	−0.51	57.75	329 000	9.10	4	3270	1.0	0.3	a
G040.29+00.19	40.29	0.19	82.82	5040	6.47	1	266	5.3	3.6	i
G040.34−00.26	40.34	−0.26	72.20	51 100	5.43	5	3950	7.7	2.6	a
G040.84−00.16	40.84	−0.16	23.74	757	1.65	5	160	21.1	10.1	a
G040.89−00.21	40.89	−0.21	26.70	–	–	1	–	–	–	–
G040.99+00.04	40.99	0.04	74.75	14 800	6.40	0	0	0.0	0.0	i
G041.04−00.26	41.04	−0.26	39.04	435 000	10.23	6	4220	1.0	0.3	i
G041.04−00.26	41.04	−0.26	65.82	15 800	4.72	4	1070	6.8	2.3	a
G041.04−00.51	41.04	−0.51	75.17	2430	6.38	0	0	0.0	0.0	i
G041.19−00.21	41.19	−0.21	59.87	291 000	8.65	14	22 600	7.8	1.6	a
G041.24−00.56	41.24	−0.56	75.60	6930	6.40	0	0	0.0	0.0	i
G041.24+00.39	41.24	0.39	71.35	2830	5.53	1	118	4.2	3.0	a
G041.29+00.34	41.29	0.34	14.81	7280	11.65	2	3360	46.2	22.1	a
G041.34−00.16	41.34	−0.16	13.54	10 700	11.70	4	4370	40.8	15.5	a
G041.34+00.09	41.34	0.09	60.30	67 100	8.55	6	4600	6.9	2.2	a
G041.59+00.29	41.59	0.29	59.02	2240	4.10	0	0	0.0	0.0	a

Table 3 – *continued*

GRS cloud name	l (°)	b (°)	V_{LSR} (km s^{-1})	M_{cloud} (M$_\odot$)	D (kpc)	No. BGPS sources	M_{clumps} (M$_\odot$)	CFE (per cent)	ΔCFE (per cent)	Arm/interarm
G041.74+00.04	41.74	0.04	17.79	56 600	11.38	4	2950	5.2	2.6	a
G041.79+00.49	41.79	0.49	41.17	71 500	9.93	0	0	0.0	0.0	i
G042.04−00.01	42.04	−0.01	57.75	243 000	8.60	8	9070	3.7	1.0	a
G042.04+00.19	42.04	0.19	18.21	3740	11.30	0	0	0.0	0.0	a
G042.09−00.11	42.09	−0.11	16.51	201	1.23	3	50.4	25.1	12.4	a
G042.14−00.61	42.14	−0.61	67.52	286 000	5.12	1	251	0.1	0.0	a
G042.14+00.09	42.14	0.09	15.66	83.8	1.17	1	45.9	54.8	28.1	a
G042.19−00.61	42.19	−0.61	34.79	1880	2.33	1	110	5.9	2.5	i
G042.29−00.51	42.29	−0.51	75.60	18 400	6.28	1	465	2.5	1.5	i
G042.34+00.39	42.34	0.39	15.24	6050	11.40	0	0	0.0	0.0	a
G042.34−00.31	42.34	−0.31	27.60	–	–	2	–	–	–	–
G042.44−00.46	42.44	−0.46	10.99	754	0.93	0	0	0.0	0.0	a
G042.44−00.26	42.44	−0.26	65.40	140 000	4.90	2	2100	1.5	0.6	a
G042.44−00.51	42.44	−0.51	33.94	898	2.28	0	0	0.0	0.0	i

Figure 1. The number of BGPS sources found in each molecular cloud with at least one association.

Figure 2. Position of the GRS clouds in the $(\theta, \ln(r))$ space, where the spiral arms are represented by straight lines. The positions of the arms are determined by the model of Vallee (1995), with the blue and grey bands representing the taken extent of the Perseus and Sagittarius arms, respectively. The clouds which fall in those arms are marked with blue and black circles, respectively, while the interarm clouds are represented with the green circles and the yellow circles denote the Scutum–Centaurus tangent clouds.

associated with less than 10 BGPS sources. Of the clouds with 10 or more, 2 are found in the interarm regions, 1 is in the Sagittarius arm and the fourth has no distance determination.

4 RESULTS AND ANALYSIS

4.1 Determining interarm clouds

In aiming to test the effect of Galactic structure on the star formation process, it is first important to distinguish between the spiral arms and interarm regions. The separation of these components is not an exact process, but the main aim is to ensure that there is sufficient separation such that the emission in each of the structure bins is dominated by sources within the main structures.

Models of the spiral structure of the Milky Way show evidence for both a two-armed model (Francis & Anderson 2012) and a four-armed model (Vallee 1995; Hou, Han & Shi 2009). However, the model of Vallee (1995) is chosen to describe the spiral-arm geometry in this study as this is the model used by Roman-Duval et al. (2009) in determining the Galactic distribution of the GRS molecular gas, which points towards a four-armed model. Hou et al. (2009) also find evidence that a four-armed model is favoured due to the distribution of H II regions and GMCs.
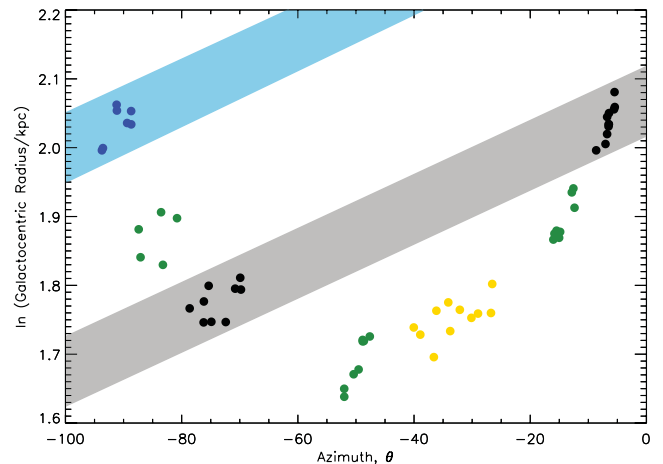
By using the model of Vallee (1995), the loci of the spiral arms (Scutum–Centaurus, Sagittarius and Perseus) are described by

$$r = 2.65 \, \text{kpc} \, e^{(\theta + \theta_0) \tan(p)}, \tag{1}$$

where r is the Galactocentric radius, θ is the azimuth around the Galactic Centre with origin located on the Galactic Centre–Sun axis, $\theta_0 = \pi$, $3\pi/2$ and 2π for the Scutum–Centaurus, Sagittarius and Perseus arms, respectively, and p is the pitch angle and is equal to 12°.7.

Making use of the kinematic velocities of each cloud in the region (Rathborne et al. 2009) and the distances to the GRS clouds (Roman-Duval et al. 2009), the Galactocentric radius and azimuth of each cloud can be calculated. Fig. 2 displays the position of each cloud in the $(\theta, \ln(r))$ space, where the spiral arms are represented by straight lines. The populations that correspond to the spiral-arm components are coloured the same as the lines, with the interarm components represented by the green circles. The clouds at $\sim -50°$ azimuth

are those at the $l = 40°$ tangent point, which is the Sagittarius–Scutum–Centaurus interarm zone (see also Sawada et al. 2012). The Scutum–Centaurus tangent clouds (those indicated by the yellow circles) do not fall on the Scutum–Centaurus arm, as indicated by the model, but are considered to be in the arm as they have the velocity distribution and distance that corresponds to the Scutum–Centaurus tangent in this line of sight. The models of the arms used here do not take into account the confusion that occurs in the bar-end/Scutum–Centaurus tangent region due to the streaming motions and large range of velocities found in this environment. Clouds were placed in the Perseus and Sagittarius arms if they fell within 0.5 kpc of the taken position of the spiral arm from equation (1).

4.2 Masses of BGPS sources

The 1.1 mm dust continuum flux densities from BGPS are converted to source masses using the standard formula:

$$M = \frac{S_\nu D^2}{\kappa_\nu B_\nu(T_d)} \qquad (2)$$

which leads to

$$M = 13.1\,M_\odot \left(\frac{S_\nu}{1\,\mathrm{Jy}}\right)\left(\frac{D}{1\,\mathrm{kpc}}\right)^2 (e^{13.12/T_d} - 1), \qquad (3)$$

where $\kappa_\nu = 0.0114\ \mathrm{cm^2\,g^{-1}}$, S_ν is the catalogued flux density, D is the source distance and B_ν is the Planck function evaluated at dust temperature T_d. A single temperature of 14 K is used for all the sources in the $l = 40°$ region, in contrast to the value of 20 K assumed by Dunham et al. (2010). The lower value is supported by the distribution of source temperatures in the $l = 40°$ region found from 70–500 μm photometry extracted from the *Herschel* infrared Galactic Plane Survey (Hi-GAL; Molinari et al. 2010) and confirmed by Veneziani et al. (2013), who found lower temperatures in the $l = 59°$ field, a field similar to the $l = 40°$ region. The BGPS sources were cross-matched with Hi-GAL detections (Schisano et al., in preparation), and the temperatures derived by spectral energy distribution (SED) and grey-body fitting (Elia, private communication). Fig. 3 shows that the peak of the temperature distribution lies at ∼14 K in both the arm and interarm components of the $l = 40°$ region
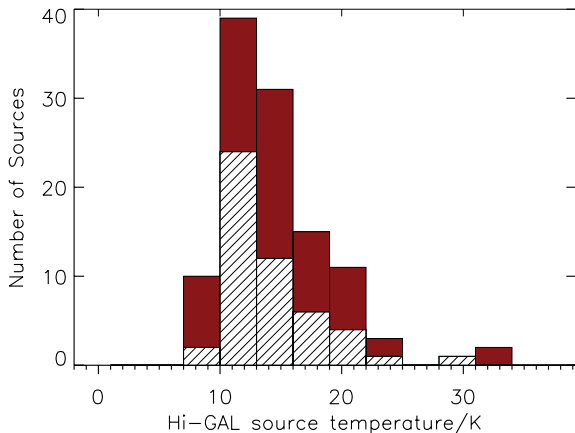

Figure 3. The distributions of SED-based temperatures of the matched Hi-GAL–BGPS sources for the $l = 40°$ region with the arm and spiral-arm components depicted by the red and white hashed bars, respectively. The regions were separated using the distances derived to the matched BGPS sources.

and this represents the most probable temperature. Allowing for a 1σ spread of the peak, clump masses may be overestimated by a factor of 1.7 or underestimated by 0.7. A Kolomogorov–Smirnov (K–S) test was applied to the T_d distributions of the two subsamples. This K–S test showed that they could be assumed to have the same temperatures as there was an 88 per cent probability that the temperatures were from the same sample. Observations of M83 by Foyle et al. (2012) found higher dust temperatures in the spiral arms compared to the interarm regions, in contrast to our results. This difference could be due to tracing a different dust mass component. At low resolutions, Foyle et al. (2012) may include a large, low-density component which is heated by the interstellar radiation field, whereas the BGPS and Hi-GAL trace dense cores that are mostly shielded by high extinction. Paradis et al. (2012) calculated the dust temperature and 500 μm emissivity excess as a function of Galactic longitude, with peaks correlating with the locations of Galactic spiral arms. However, this is at a resolution of 4 arcmin and will include diffuse emission, while we use extracted point sources and exclude the diffuse material.

It should also be noted that absolute masses and accurate distances are not vital to most of the results in this study since we are mainly concerned with mass ratios (Section 4.3) in which case uncertainties in distance are not an issue. Reliable associations between BGPS sources and molecular clouds are much more important and the separation into the different populations identified with Galactic structures can be achieved with source velocities alone.

4.3 Clump formation efficiencies

The clump formation efficiency (CFE) is a measure of the fraction of molecular gas that has been converted into dense, potentially star-forming clumps. This quantity is analogous (or is a precursor) to the SFE. The CFE must be viewed as an upper limit to the SFE or the first step in a sequence of conversion efficiencies from molecular clouds to stars.

The CFE is a measure of

$$\frac{M_{\mathrm{clump}}}{M_{\mathrm{cloud}}} = \frac{1}{M_{\mathrm{cloud}}} \int_0^t \frac{dM}{dt}\,dt, \qquad (4)$$

where dM/dt is the instantaneous clump formation rate. A high value for the CFE can indicate either a high clump formation rate or a long formation time-scale.

Using the catalogued GRS cloud masses (Roman-Duval et al. 2010) and the derived masses for the BGPS sources, we are able to calculate total CFEs for the different velocity components of the $l = 40°$ field. The total CFEs also include the masses of the unassociated BGPS sources, which were assigned to populations by the same method used to assign clouds as they have velocities and derived kinematic distances, and the GRS clouds with no associated BGPS sources. The total CFE values for the spiral-arm and interarm regions, respectively, are 5.5 ± 0.6 and 4.9 ± 0.7 per cent. The individual spiral arms had total CFEs of 2.0 ± 0.4, 4.3 ± 0.5 and 36.3 ± 9.0 per cent for the Scutum–Centaurus, Sagittarius and Perseus arms, respectively, with the individual interarm regions having CFEs of 15.8 ± 2.9, 2.3 ± 0.5 and 6.5 ± 1.0 per cent. These interarm regions are listed in the order of decreasing azimuthal angle, as indicated in Fig. 2. These values do not include the masses of the small, low-velocity-dispersion clouds discussed in Section 3.1 that were not included by Rathborne et al. (2009), and as such the CFEs can be taken as an upper limit. The uncertainties on the CFEs are a combination of the catalogued GRS cloud mass uncertainties (Roman-Duval et al. 2010), the uncertainties in

BGPS flux densities (Rosolowsky et al. 2010) and the distribution of source temperatures, using the variance of the distribution. Any biases corresponding to the distance distribution of cloud masses are discussed in detail by Roman-Duval et al. (2010). The total CFE values obtained for spiral-arm and interarm clouds are consistent within the uncertainties. In the separated spiral-arm components, the CFE in the Perseus arm shows a large increase, significant at the 3σ level.

The CFE calculations are based on the molecular mass accounted for in the catalogue of Roman-Duval et al. (2010) and all the BGPS-traced mass with a known velocity, both with and without an associated CO mass. The 24 BGPS sources without an associated cloud make up 12 per cent of the 196 sources and only 6 per cent of the total clump mass. The molecular mass not counted in the filamentary clouds and small, low-velocity-dispersion clouds makes up some small part of the 37 per cent of the total molecular mass in the GRS data not picked up by the CLUMPFIND search of Roman-Duval et al. (2009). As a result, combining these two effects, we can say that inclusion of the clump masses without an associated molecular mass does not significantly bias the CFE values.

5 DISCUSSION

5.1 Interarm star formation

Determining the quantity of ongoing star formation in the interarm regions is key to understanding how important the spiral arms are in the overall production of stars and what effect, if any, they have on the SFR. Studies of other galaxies have shown higher SFEs in the spiral arms compared to interarm regions in Hα fluxes and H$\,$I (e.g. Cepa & Beckman 1990; Seigar & James 2002). However, Bigiel et al. (2008) and Blanc et al. (2009) have argued that the SFR correlates with CO intensity and the surface density of the molecular gas, as opposed to the H$\,$I component.

The total SFR in a molecular cloud or galaxy is directly related to, and possibly determined by, the amount of dense molecular gas it contains. SFRs and total molecular masses are correlated over nine orders of magnitude in mass scale and can be described by a family of linear scaling laws, parametrized by the fraction of molecular gas that is dense (i.e. $n(H_2) > 10^4$ cm^{-3}). That is, the underlying star formation scaling law is always linear for systems with the same dense gas fraction (Lada et al. 2012). It is also shown that the SFR is linear on scales from Galactic GMCs to sub-millimetre galaxies above a density threshold (Krumholz, Dekel & McKee 2012).

By defining the SFE in terms of the ratio of SFR, derived from both the far-ultraviolet and 24 μm emission, to the H$_2$ surface density, Foyle et al. (2010) found no enhancement in the molecular fraction of total gas mass, nor in the SFE compared to interarm regions, in the arms of two external spiral galaxies, with SFE variations found to be set by local environmental factors (Bigiel et al. 2008). By taking the CFE to be as analogous to the SFE, we can say that this is consistent with the results of this study. The median cloud CFEs are 5.6 ± 3.1 and 5.3 ± 3.3 per cent for the arm and interarm regions, respectively, where the uncertainties are the median absolute deviations. The mean cloud CFEs are 14.9 ± 4.8 and 16.3 ± 7.5 per cent, respectively. The two samples are displayed in Fig. 4 and a K–S test shows that there is a 58 per cent probability that they are from the same population. So, neither the total CFEs nor those for the individual groups of clouds show any evidence of systematic difference with Galactic environment.

However, there are significant variations from cloud to cloud, as seen in Fig. 4, but they are part of a single population. This is consis-
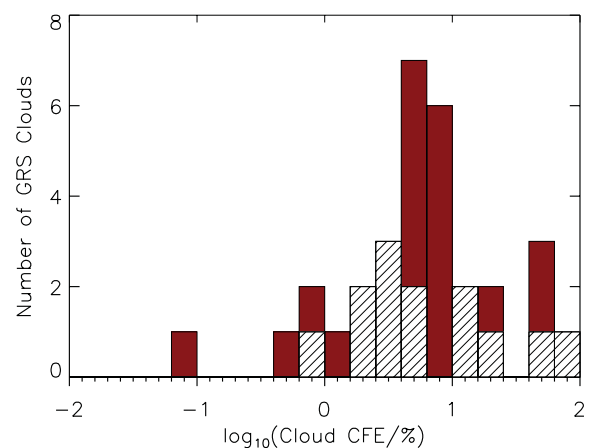

Figure 4. Distribution of the CFEs for individual GRS clouds with the spiral-arm and interarm components depicted by the red and white hashed bars, respectively.

tent with Eden et al. (2012) and suggests that local feedback on the scale of individual clouds is the dominant process in determining CFE or SFE changes.

The total CFEs for the interarm regions indicate that there is both inefficient and efficient star formation going on in the interarm regions as well as in the spiral arms. CFEs in the individual clouds, as shown in Fig. 4, show that high-CFE clouds are found both in the interarm and spiral arms. Three of the five clouds with a CFE found to be greater than 40 per cent are associated with an H$\,$II region. The presence of these H$\,$II regions could be the cause of the increase due to the correlation between feedback processes and an increase in SFE (e.g. Moore et al. 2007).

There is evidence that the $l = 40°$ line of sight is host to a Galactic spur (Weaver 1970; Shane 1972) between the Sagittarius and Scutum arms. These interarm spurs are observed in external galaxies (e.g. Corder et al. 2008; Muraoka et al. 2009), with the spurs in M51 and M83 well correlated with interarm H$\,$II regions and sites of massive star formation. This region, which we have counted as interarm, is found to have a much lower CFE than the total interarm region at 2.3 ± 0.5 per cent. Thus, its inclusion cannot bias the results in the sense of producing an artificially high CFE for the interarm zones. Sakamoto et al. (1997) found that there was a lower than average gas density in this region, implying that this spur is not of a similar gas density to spiral-arm gas, and no enhancement compared to other interarm regions.

5.2 Star formation in the Perseus arm

Moore et al. (2012) found that the infrared luminosity-to-cloud mass ratio, in the sector of the Galactic plane covered by the GRS, was significantly increased in the Perseus arm, compared to the Scutum–Centaurus tangent, the Sagittarius arm and adjacent interarm regions. However, this increase could be entirely accounted for by the presence of the W49A massive star-forming region, a promising Galactic analogue for an extragalactic starburst system with dust temperatures >100 K and densities $>10^5$ cm^{-3} (Nagy et al. 2012).

The $l = 40°$ region is a subset of the area studied in Moore et al. (2012) but W49A is not included here. However, we do still find a peak in CFE in the Perseus arm clouds, as can be seen in Fig. 5. The total CFE for spiral-arm regions is marked with the dashed line.
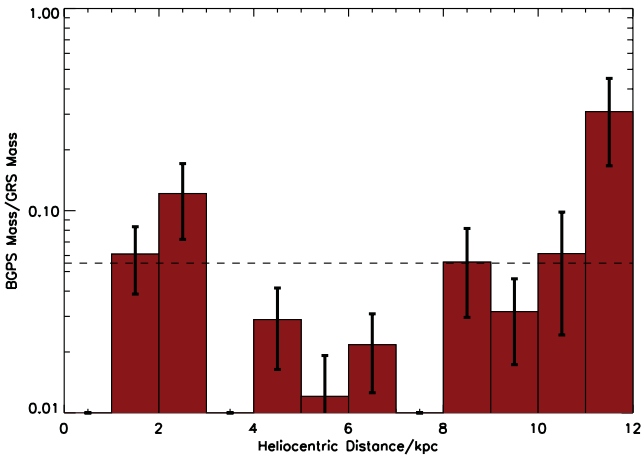
Figure 5. The total CFE as a function of the heliocentric distance within the $l = 40°$ region, with the Perseus arm found at 11.0–12.0 kpc. The dashed line indicates the total CFE for spiral-arm regions.

Figure 6. The total CFE as a function of Galactocentric radius within the $l = 30°$ region, outlined in Eden et al. (2012), and the $l = 40°$ region. Sources with heliocentric distance less than 2 kpc are omitted, in order to remove local sources that might affect the results at Galactocentric radii of $\sim$8 kpc.

There is a peak in the CFE at the heliocentric distance associated with the Perseus arm (11.0–12.0 kpc at $l = 40°$) and the total CFE for the Perseus arm clouds is found to depart at the 3σ level from that in the other zones, with a CFE of 36.3 ± 9.0 per cent. The uncertainties are the uncertainties described in Section 4.3, with a Poisson consideration on the number of GRS clouds. This increase is possibly still the effect of W49A ($l = 43°.17$ which falls outside the $l = 40°$ region), but this would require it to be doing so at a scale of $\sim$800 pc, if we assume a distance of 11.4 kpc (Gwinn, Moran & Reid 1992). Increases in the CFE related to triggering from feedback have been observed (Moore et al. 2007) but only on the scale of tens of parsecs. It is unlikely that an individual star-forming region would have an effect at this distance although it may be that the peripheral clouds around W49A itself may also have abnormally high CFE.

As mentioned in Section 4.3, the high CFE implies either a high clump formation rate or a long formation time-scale. However, as the clump stage is shown to be short, $\sim$0.5 Myr (e.g. Ginsburg et al. 2012), this increase is more likely to be due to an increased formation rate in this spiral arm as it would otherwise require much more extended dense-clump lifetimes, for which there is no evidence.

Roman-Duval et al. (2010) suggest that the GRS survey may be undersampled at the distance of the Perseus arm, mainly because the arm was not as clearly defined as other arms in the cloud distribution. If this were the case, it would result in artificially elevated CFE values and bring the result discussed above into question. However, there is no direct evidence for undersampling and other data at similar Galactocentric radii have also revealed spiral arms that are poorly defined in star formation tracers (e.g. Urquhart et al. 2013). The BGPS traces mass further than the catalogued clouds of the GRS; however, by removing the sources with a heliocentric distance further than the furthest GRS cloud, the Perseus CFE still remains elevated at 31 per cent.

5.3 The scales of star formation

The formation of stars is an evolutionary and hierarchical process. Molecular clouds form from atomic gas and these clouds form internal dense clumps within which cluster-sized systems form, and which in turn house cores where single stars or small multi-star systems are produced. Each of these stages is subject to its own
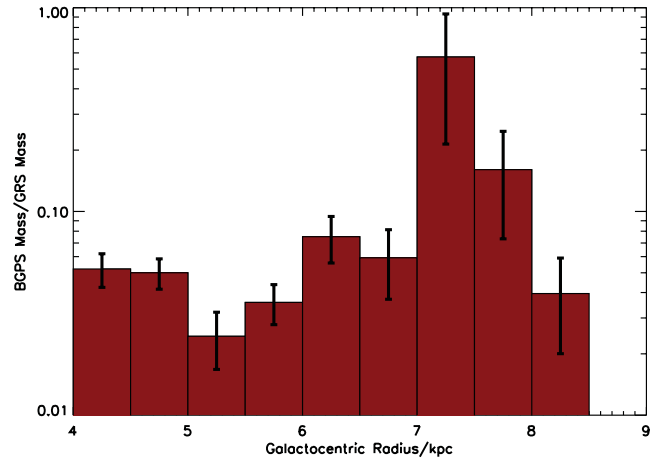
efficiency, each of which can be measured. The formation efficiency of molecular clouds can be obtained from the ratio of H_2 to H I mass, and that of the star-forming clumps from clouds is measured by the CFE discussed here and the conversion of stars out of the gas from the infrared luminosity-to-cloud or clump mass.

If the environment pertaining to large-scale structure were changing the star formation process, at least one of these efficiencies should show some variation with environment on kpc scales. The work of Foyle et al. (2010) has shown no variation between the interarm and arm regions in the ratio of molecular to atomic gas, albeit only in two spiral galaxies. This study, as well as that of Eden et al. (2012), has shown no evidence that the CFE is dependent on proximity to spiral arms or varies between arms. Fig. 6 displays the CFE as a function of Galactocentric radius, combining the results of this study and Eden et al. (2012). However, it has been found that the ratio of the integrated YSO luminosity to molecular cloud mass is influenced by the presence of some, but not all, spiral-arm structures (Moore et al. 2012). This implies that the clump-to-stars stage is affected by spiral structure, but it is unclear as to how this occurs.

6 CONCLUSIONS

By associating 196 BGPS sources to GRS clouds with known distances, and using the rotation curve of Brand & Blitz (1993) combined with kinematic velocities, we assigned kinematic distances to 196 BGPS sources found in the Galactic plane slice from $l = (37°.83–42°.50)$, $|b| \leq 0°.5$.

The distances and kinematic velocities of the GRS clouds (Rathborne et al. 2009; Roman-Duval et al. 2009) were inverted to give Galactocentric radii and azimuthal angles, allowing for clouds to be located in terms of arm and interarm material, and by separating the clouds into these two groups, we are able to test how the CFE varies with Galactic environment.

The CFEs, defined as the clump-to-cloud mass ratio, were found to be 5.5 ± 0.56 and 4.9 ± 0.7 per cent for the combined arm and interarm regions, respectively, hence consistent with each other. The CFEs for the individual arms are 2.0 ± 0.4, 4.3 ± 0.5 and 36.3 ± 9.0 per cent for the Scutum–Centaurus, Sagittarius and Perseus arms, respectively.

The median cloud CFEs for the arm and interarm regions are 5.6 ± 3.1 and 5.3 ± 3.3 per cent, respectively, with corresponding mean values of 14.9 ± 4.8 and 16.3 ± 7.5 per cent. These are also consistent with each other.

The work of Foyle et al. (2010), Eden et al. (2012) and Moore et al. (2012), combined with this study, shows that that the large-scale structure does not seem to change the efficiency of the formation of the clouds or clumps from which stars form and any increases in SFE may come from the conversion of clumps to stars.

ACKNOWLEDGEMENTS

REFERENCES

Aguirre J. E. et al., 2011, ApJS, 192, 4
Anderson L. D., Bania T. M., 2009, ApJ, 690, 706
Benjamin R. A. et al., 2005, ApJ, 630, L149
Bigiel F., Leroy A., Walter F., Brinks E., de Blok W. J. G., Madore B., Thornley M. D., 2008, AJ, 136, 2846
Binney J., Gerhard O. E., Stark A. A., Bally J., Uchida K. I., 1991, MNRAS, 252, 210
Blanc G. A., Heiderman A., Gebhardt K., Evans N. J., II, Adams J., 2009, ApJ, 704, 842
Blitz L., Spergel D. N., 1991, ApJ, 379, 631
Brand J., Blitz L., 1993, A&A, 275, 67
Buckle J. V. et al., 2009, MNRAS, 399, 1026
Cepa J., Beckman J. E., 1990, A&A, 239, 85
Clemens D. P., Sanders D. B., Scoville N. Z., Solomon P. M., 1986, ApJS, 60, 297
Corder S., Sheth K., Scoville N. Z., Koda J., Vogel S. N., Ostriker E., 2008, ApJ, 689, 148
Dib S., Walcher C. J., Heyer M., Audit E., Loinard L., 2009, MNRAS, 398, 1201
Dobbs C. L., Bonnell I. A., Pringle J. E., 2006, MNRAS, 371, 1663
Dobbs C. L., Burkert A., Pringle J. E., 2011, MNRAS, 417, 1318
Dunham M. K. et al., 2010, ApJ, 717, 1157
Dwek E. et al., 1995, ApJ, 445, 716
Eden D. J., Moore T. J. T., Plume R., Morgan L. K., 2012, MNRAS, 422, 3178
Foyle K., Rix H.-W., Walter F., Leroy A. K., 2010, ApJ, 725, 534
Foyle K. et al., 2012, MNRAS, 421, 2917
Francis C., Anderson E., 2012, MNRAS, 422, 1283
Ginsburg A., Bressert E., Bally J., Battersby C., 2012, ApJ, 758, L29
Gwinn C. R., Moran J. M., Reid M. J., 1992, ApJ, 393, 149

Hammersley P. L., Garzón F., Mahoney T. J., López-Corredoira M., Torres M. A. P., 2000, MNRAS, 317, L45
Heyer M. H., Terebey S., 1998, ApJ, 502, 265
Hou L. G., Han J. L., Shi W. B., 2009, A&A, 499, 473
Jackson J. M. et al., 2006, ApJS, 163, 145
Krumholz M. R., Cunningham A. J., Klein R. I., McKee C. F., 2010, ApJ, 713, 1120
Krumholz M. R., Dekel A., McKee C. F., 2012, ApJ, 745, 69
Lada C. J., Forbrich J., Lombardi M., Alves J. F., 2012, ApJ, 745, 190
Lépine J. R. D. et al., 2011, MNRAS, 417, 698
Molinari S. et al., 2010, A&A, 518, L100
Moore T. J. T., Bretherton D. E., Fujiyoshi T., Ridge N. A., Allsopp J., Hoare M. G., Lumsden S. L., Richer J. S., 2007, MNRAS, 379, 663
Moore T. J. T., Urquhart J. S., Morgan L. K., Thompson M. A., 2012, MNRAS, 426, 701
Muraoka K. et al., 2009, ApJ, 706, 1213
Nagy Z., van der Tak F. F. S., Fuller G. A., Spaans M., Plume R., 2012, A&A, 542, A6
Paladini R., Davies R. D., De Zotti G., 2004, MNRAS, 347, 237
Paradis D. et al., 2012, A&A, 537, A113
Rathborne J. M., Johnson A. M., Jackson J. M., Shah R. Y., Simon R., 2009, ApJS, 182, 131
Roman-Duval J., Jackson J. M., Heyer M., Johnson A., Rathborne J., Shah R., Simon R., 2009, ApJ, 699, 1153
Roman-Duval J., Jackson J. M., Heyer M., Rathborne J., Simon R., 2010, ApJ, 723, 492
Rosolowsky E. et al., 2010, ApJS, 188, 123
Russeil D., 2003, A&A, 397, 133
Sakamoto S., Hasegawa T., Handa T., Hayashi M., Oka T., 1997, ApJ, 486, 276
Sanders D. B., Clemens D. P., Scoville N. Z., Solomon P. M., 1986, ApJS, 60, 1
Sawada T., Hasegawa T., Sugimoto M., Koda J., Handa T., 2012, ApJ, 752, 118
Seigar M. S., James P. A., 2002, MNRAS, 337, 1113
Shane W. W., 1972, A&A, 16, 118
Stil J. M. et al., 2006, AJ, 132, 1158
Urquhart J. S. et al., 2007, A&A, 474, 891
Urquhart J. S. et al., 2013, preprint (arXiv:1302.2538)
Vallee J. P., 1995, ApJ, 454, 119
Veneziani M. et al., 2013, A&A, 549, A130
Weaver H., 1970, in Becker W., Kontopoulos G. I., eds, Proc. IAU Symp. Vol. 38, The Spiral Structure of Our Galaxy. Reidel, Dordrecht, p. 126
Williams J. P., de Geus E. J., Blitz L., 1994, ApJ, 428, 693

SUPPORTING INFORMATION

Additional Supporting Information may be found in the online version of this article:

Table 1. Summary of GRS cloud parameters and BGPS source associations (http://mnras.oxfordjournals.org/lookup/suppl/doi:10.1093/mnras/stt279/-/ DC1).

Please note: Oxford University Press are not responsible for the content or functionality of any supporting materials supplied by the authors. Any queries (other than missing material) should be directed to the corresponding author for the article.

This paper has been typeset from a TEX/LATEX file prepared by the author.